Cycloidal stepper motor: a systematic approach for designing a non-magnetic rotary actuator

Haipeng Liang, Zion Tse

School of Engineering and Materials Science, Queen Mary University of London, London, E1 4NS

Abstract–Magnetic resonance imaging (MRI) has the ability to provide high-quality images of soft tissues, and obtain the positions of surgical tools and target tissues, which is extremely useful in minimally invasive surgery. Hence, there is a significant need for surgical robots capable of working in the MRI environment, but designing MR-conditional actuators is one of the biggest obstacles to developing such robots.

This study provides a novel approach to building pneumatic motors. A gear set design inspired by the curtate hypocycloid is applied for the motion of the rotor. The motor's operating principle and mechanical design including rotor and housing are presented. The relationship between different transmission ratios and motors is explored, showing that motors with more chambers and higher resolution can be obtained based on this hypocycloid. A physical prototype is made by 3D printing and laser cutting, and experimental data shows that the presented motor can achieve a maximum speed of 2000 rpm and a torque of 11 mN·m.

Keywords — **MRI, Pneumatic stepper motor, MR-conditional.**

I. INTRODUCTION

Medical imaging modalities such as ultrasound, magnetic resonance imaging (MRI), and computed tomography (CT) have the ability to provide accurate positional relationships between anatomical regions and surgical instruments. Therefore, they have been widely used for clinical diagnosis [1], surgical navigation, and treatment, allowing surgeons and surgery support systems to conduct surgeries less invasively [2]. Unlike other imaging techniques, MRI does not require the use of ionizing radiation and provides excellent contrast between various soft tissues with high resolution and good quality [3]. For this reason, surgery-support systems that can be used inside MRI scanners have been developed rapidly. Some examples include needle surgery-support systems for prostate ablation [4, 5], needle biopsy, and liver cancer.

The working principle of MRI is the use of a strong magnetic field to map the locations of soft tissues. Thus, ferromagnetic materials, which can pose hazards to patients and devices under strong magnetic fields, are prohibited from being used in MRI scan rooms. Besides, the use of paramagnetic materials, which can produce interference and artifacts during the imaging process, should be restricted [6]. The American Society for Testing and Materials (ASTM) introduced two terms to describe devices based on their response to the magnetic field generated by MR scanners: MR safe and MR conditional [7]. MR-safe devices pose no hazards to patients or surgeons under all MR environments, whereas MR-conditional devices pose no known hazards under specified conditions.

Electric motors use electricity to generate electromagnetic power, and noise from electronic circuits can considerably degrade the signal-to-noise ratio (SNR) of MR images [8]. Therefore, electric motors cannot be used inside MRI scan rooms. Piezoceramic actuators contain no magnetic materials and are MR-conditional, so they are often substituted for electric motors. However, the electric current driving the actuators produces heat and induces electromagnetic interference, thus lowering the quality of MR image [5]. Hydraulic actuators are another option for MR-conditional robots, but the possibility of liquid leakage, no matter how little, may not be acceptable in medical applications [9, 10].

Compared to piezoceramic and hydraulic actuators, pneumatic actuators are a more promising method for MR-conditional robots. MRI scan rooms are often equipped with compressed air supplies, which can be utilized to operate pneumatic actuators. Components like pistons, bearings, and air hoses can easily be made MR-conditional. When air leakage occurs inside the MRI scanner, it will not pose a hazard or negatively affect the working of the MR scanner, and unlike water leakage from hydraulic actuators, air leakage poses no hazard to the medical environment [9]. Furthermore, pneumatic actuators cause little interference in MR images. For these reasons, pneumatic actuators have attracted much interest for their potential use in MR-conditional robots.

Because of the compressibility of air, the accurate position control of pneumatic MR-conditional motors is difficult. Therefore, position feedback is needed to get closed-loop control [11]. However, components like sensors, encoders, and fibers used for feedback must be MR-conditional [12]. Moreover, control approaches are needed for the control of the actuators [13]. All of these additions to the motors complicate the robot system. As a possible solution, stepper motors work step by step, achieving excellent position control without the incorporation of feedback components.

Table 1. Comparison of some existing pneumatic stepper motors with the proposed pneumatic motor.

Reference	Number of parts	Size (mm)	Resolution	Torque	Maximum speed
Sajima et al. [14]	~ 10	Φ30 × 40	4.29°	150 N·mm at 0.6MPa	48 rpm
Secoli et al. [15]	~ 10	250 × 250 × 50	60°	400 N·mm at 10.8 rpm	180 rpm
Stoianovici et al. [16]	> 20	Φ85 × 30 × 30	3.33°	650 N·mm at 120 psi	166.6 rpm
Groenhuis and Stramigioli [17] (R80 motor)	~ 10	80 × 80 × 37	10°	3.7 N·m at 0.49 MPa	133 rpm
Boland et al. [18]	15	80 × 80 × 80	90°	19 N·mm	2000 rpm
The present study	7	Φ68 × 25	60°	11 mN·m	2000 rpm

Table 1 presents the parameters of a number of existing stepper motor designs alongside the proposed design. Sajima et al. developed a Pneumatic Rotation Stepping Actuator [14]. By controlling the air in three cylinders, three direct acting gears drive the rotation gear to rotate. The maximum torque of the motor is 150 mN·m. The three-piston motor developed by Secoli et al. has an output torque of 400 mN·m at a speed of 10.8 rpm [15], but it has the largest size among the compared motors, which limits its applications in robot designs. PneuStep, developed by Stoianovici et al., is a stepper motor driven by three ports of pressured air with an output power of 37 W [16], but it has the most components among these motors, making the assembling process difficult. Groenhuis and Stramigioli [17] applied teeth to the motors and proposed both rotary and linear motors, including R-80, which has the strongest output torque among the compared motors. Using the wedge mechanism, Groenhuis et al., recently proposed a new pneumatic motor [19], which can achieve multi-axis outputs and has the potential to be applied in a robot platform with simplified driving parts. A stepper motor proposed by Boland et al. uses four cylinders to control the movement of the shaft [18] by controlling the compressed air in each cylinder in a sequential manner. Although it can reach a maximum of 2000 rpm, the large number of parts complicates the assembly.

This study proposes a new approach to designing pneumatic stepper motors, in which the motor is designed according to the generation of a hypocycloid. With a planetary gear set, the rotor can rotate in an expected way. By changing the transmission ratio, motors with different shapes and resolutions can be obtained. Unlike some pneumatic stepper motors, which have many cylinders and pistons, the proposed motor only has a rotor, and a housing separated into several chambers. So, the motor is composed of less than 10 pieces, having the fewest number of components among compared motors, which makes it easy to assemble.

II. METHODS AND MATERIALS

A. Working Principle

A hypocycloid is a special plane curve generated by the trace of a fixed point on a small circle that rolls within a large circle. W is the radius of the large circle, r is the radius of the small circle, and the radius ratio is $j = W / r$ (Assuming $j > 1$). With different ratios, curves with different cusps can be obtained. A hypocycloid with three cusps is known as a deltoid, and a hypocycloid with four cusps is known as an asteroid. The shapes of hypocycloids with different ratios are shown in Fig. 1. Moreover, the trajectories of the points on a small circle with a radius of $(j - 1) \cdot r$ and $j \cdot r$ are the same.
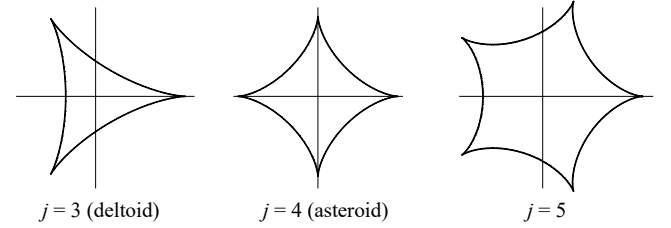

Fig. 1. The shapes of hypocycloids with different ratios.

When j is an integer, the curve is closed and the point runs around the center of the large circle at an angular speed of ω, while it is rotating around the small circle at an opposing angular speed of $j \cdot \omega$. Thus, the position of the cusp on the outline (x, y) can be written as:

$$\begin{cases} x = r(j-1) \cdot \cos \beta + r \cdot \cos((j-1)\beta) \\ y = r(j-1) \cdot \sin \beta - r \cdot \sin((j-1)\beta) \end{cases} \quad (1)$$

where β is the rotation angle of the small circle center around the large circle center.
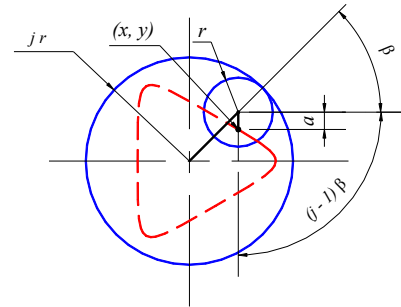

Fig. 2. Parameters of the cusp in a hypocycloid.

Furthermore, the radius of the cusp inside the small circle is a, shown in Fig. 2. When $a < r$, the trajectory of the cusp inside the small circle rolling on a larger circle is called a curtate hypocycloid. When $a > r$, the trajectory of the cusp outside the small circle is called a prolate hypocycloid. Fig.

3 shows the traces of a standard hypocycloid, a curtate hypocycloid, and a prolate hypocycloid, respectively. The prolate hypocycloid (a > r) is self-intersecting, making the physical realization impossible. The curtate hypocycloid (a < r) has smoother corners and no overlapping sections, so the cusps always move inside the chamber, making the physical realization possible. Therefore, in this study, the motor is built according to the curtate hypocycloid.
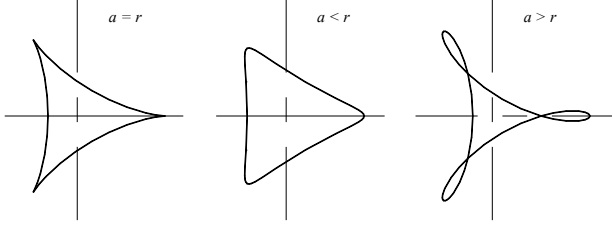
(a) Standard hypocycloid   (b) Curtate hypocycloid   (c) Prolate hypocycloid

Fig. 3. The shapes of hypocycloids with different radius variation ratios.

In the generation of the hypocycloid, the rotation speed of the small circle is proportional to the revolution speed of the carrier. Based on this, a planetary gear set is used to drive the rotation and revolution of the cusp inside the small circle. As shown in Fig. 4, a ring gear and a planet gear are used in this system. The ring gear is fixed, whereas the planet gear is mounted on a carrier (the eccentric shaft) that rolls around the ring gear. The eccentricity of these two gears is written as $e = R - a$, where R is the radius of the ring gear, and a is the radius of the planet gear. The radius variation ratio can be presented as $k = a / e$.
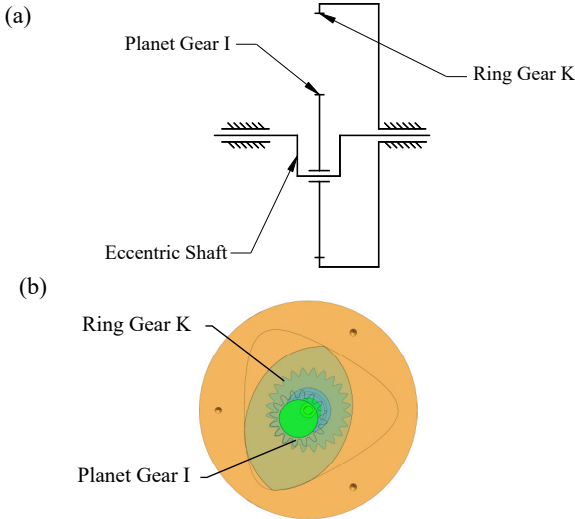

Fig. 4. (a) The outline of the planet gear set. (b) The planet gear set in the motor.

The transmission ratio can be expressed as:

$$i_H = \frac{n_K - n_H}{n_I - n_H} = \frac{Z_I}{Z_K} \quad (2)$$

where n_H, n_K, and n_I are the rotation speeds of the eccentric shaft, ring gear, and planet gear, respectively, and Z_K and Z_I

are the teeth numbers of the ring gear and planet gear. The ring gear is fixed, so $n_K = 0$. The eccentricity e can be presented as:

$$e = \frac{m \cdot Z_K - m \cdot Z_I}{2} \quad (3)$$

Let $Z_K = 24$, $Z_I = 16$, and $m = 1$. Then, the eccentricity can be calculated to be 4, and the transmission ratio is:

$$i = \frac{n_H}{n_I} = -2 \quad (4)$$

In equation(4), the transmission ratio is negative. This is because the rotation direction is opposite to the revolution direction.

Fig. 4a shows the outline of the gear set in the motor. In this design, the ring gear K is fixed on the housing, and the planet gear I rotates around it. Fig. 4b shows the gear set in the proposed motor.

With the gear set, a rotor mounted with a spur gear is applied to mimic the motion of the cusps. The rotor revolves around the motor center, while it is rotating around itself. The outline of the inner wall of the motor's housing is the hypocycloid. Fig. 5a, 5b show the CAD design and the photo of the stepper motor.
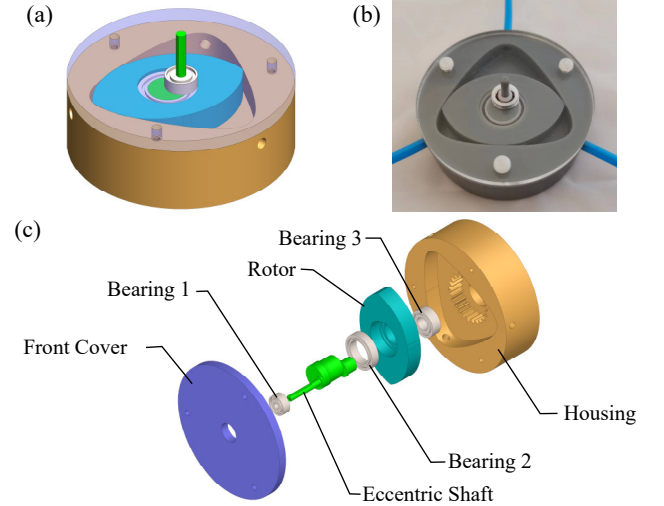

Fig. 5. (a) CAD drawing of the stepper motor. (b) Photo of the motor. (c) Exploded view of the 3-chamber motor.

B. Motor Design

Fig. 5c shows the exploded view of the proposed 3-chamber motor. This motor has a simple structure, consisting of only four fabricated parts. The rotor was fabricated with the spur gear mounted in the back. The three main components—the eccentric shaft, housing, and rotor—were constructed from 3D printing resin. They were printed by Form 3+ using stereolithography (SLA) technology which can produce strong and airtight parts. The cover was made with a laser cutter machine, using clear polymethyl methacrylate (PMMA) to get a clear view of the rotor's motion. When the motor works, the rotor runs with the planet gear simultaneously. As Formlabs 3+ has an accuracy of 25um, the tolerance between the rotor and the housing is around 50 or 100 um to minimize air leakage. Compressed

air is supplied through three channels around the housing wall, positioned 120° apart from the motor center. To minimize the friction between the moving parts, Vaseline was applied to the gear set and the gaps between the rotor, housing, and cover.

To meet the requirement of MR safety, all the materials used in the motor have to be MR-conditional. The fabrication techniques and materials of the motor are listed in Table 2.

Table 2. The fabrication techniques and materials of the motor

Item	Fabrication technique	Material
Front Cover	Laser cutting	PMMA
Eccentric Shaft	3D printing	Resin
Rotor	3D printing	Resin
Housing	3D printing	Resin
Bearing1	Plastic (623)	Polyamide and glass
Bearing2	Plastic (6701)	Polyamide and glass
Bearing3	Plastic (687)	Polyamide and glass

The motor has the dimensions of Φ 68 × 25 mm, and the parameters of the motor are shown in Table 3.

Table. 3 Definitions of parameters

Parameter	Description	Value
D	Outer diameter of the motor	68 mm
H	Height of the motor	25 mm
i	Transmission ratio	-2
e	Eccentricity	4 mm
a	Rotor major axis radius	24 mm
k	Radius variation ratio	6
h	Height of the rotor	8 mm
Z_K	Teeth number of the ring gear	24
Z_I	Teeth number of the inner gear	16
m	Modulus of the gear	1 mm

C. Working Sequence

As a stepper motor, the motor is driven by regulating the air pressures in different chambers. At the start of one step, the pressured air injected into one chamber generates the force applied to the rotor. Because of the eccentricity e, there will be a torque generated on the shaft. As the rotor rotates, the moment arm decreases, until it reaches the end of this step, where the moment arm is zero.

Fig. 6 shows the working sequence of the motor running for one cycle. Three 3-way 2-position solenoid valves are used for the control of the air in three chambers. When the valve is activated, the relevant chamber will be filled with pressured air. Otherwise, the port connected with this chamber will become an exhaust to let the air inside escape. When port A is activated, compressed air in chamber A will

generate a torque to drive the rotor to rotate clockwise (Fig. 6a) until it arrives at the end position of this step, at which point it begins to hold its position (Fig. 6b). During this time, the air in chamber B and chamber C exhausts from port B and port C. Meanwhile, the output shaft is rotating counter-clockwise. After this step is finished, port A becomes an outlet and port B becomes an inlet, and compressed air in chamber B drives the rotor to rotate continuously, allowing the air in the other two chambers to exhaust from port A and port C (Fig. 6c, 6d). Similarly, when the second step is finished, pressured air in chamber C drives the rotor to move continuously. Port C becomes an inlet, and the other two ports become outlets (Fig. 6e, 6f). In summary, the compressed air in the three chambers is activated sequentially when the motor works, and there is always one chamber activated during the rotation.
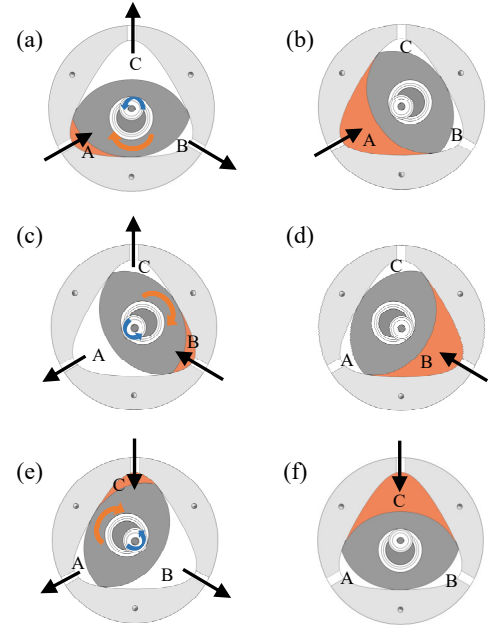

Fig. 6. (a-f) One cycle of the motor's operation. The amber shading means the chamber is energized, and the black arrows show the airflow direction. The amber and blue arrows represent the rotating directions of the rotor and output shaft, respectively.

In the proposed motor, one step movement of each chamber may drive the output shaft to revolve one-third of a cycle (120°), suggesting that the motor's resolution is 120°. The air in two chambers can work together to hold a midway position, which allows two chambers to operate on the rotor at the same time, generating smoother movement. As a result, each step can force the shaft to revolve one-sixth of a cycle (60°). Thus, the working sequence of the pressured air in chambers during one cycle is as follows:

CA → A → AB → B → BC → C

Fig. 7 shows two steps' worth of movement of the motor running at 6 steps/cycle with a holding position, and the air pressure states of each chamber are depicted in Fig.8.
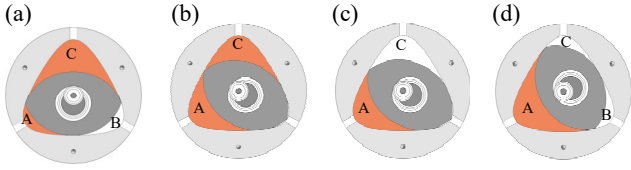
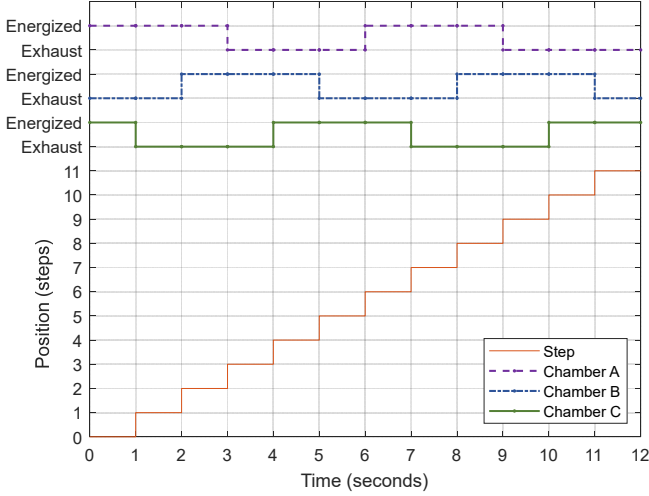Fig. 7. (a - d) The motor working at 6 steps/cycle with activation of more than one chamber at a time.

Fig. 8. Position graph of the motor running at 6 steps per cycle at 1 step/s and the corresponding chambers' states.

For the motor running at 6 steps/cycle, at the start position, the torque generated by air in chamber A is greater than that in chamber C due to the moment arm difference, driving the rotor to revolve. As the rotor rotates, the torque from chamber A decreases, and that from chamber C increases until they become equal at 60°, where the areas of chamber A and C are identical, as shown in Fig. 7b.

When two chambers are operating together (from Fig. 7a to Fig. 7b), the torque created by chamber C is opposite to the rotation of the shaft, resulting in a reduction in output torque. Technically, the output torque of the motor working at 6 steps/cycle is weaker than that working at 3 steps/cycle.

D. Rotor Design

As the edge number of the rotor is less than that of the housing, at least one of the rotor's edges has to be in contact with the inner wall of the housing at any given time to have a closed chamber. Fig. 9 shows the working statuses of the motor when the rotor is at the start and middle step positions. The cusps in blue are the two fixed dots on both sides of the rotor, while the points in red are the moving dots on the rotor's edge which are in contact with the inner wall of the housing. At the start positions of one step (Fig. 9a), point Y and cusp Z1 are merged, point X on the lower edge is in contact with the inner wall of the housing, and chambers B and C are closed to let compressed air in. As the rotor rotates counter-clockwise, the contact point X moves to the left. At the same time, another point Y starting from cusp Z1 moves to the right alongside the upper edge. When the rotor moves to the middle position of this step (Fig. 9b), two points on

each edge are in contact with the inner wall of the housing. The two points stop the compressed air in one chamber from getting into the other two chambers. As a result, the rotor is driven to rotate by the air in the closed chambers.
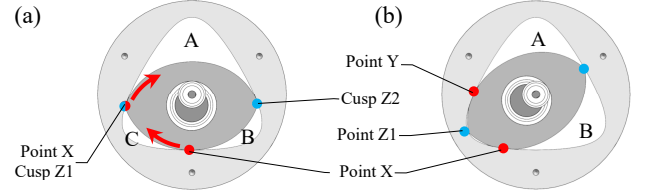

Fig. 9. (a) Start of one step showing the positions of the cusps and points. (b) Middle position of the step. The arrows show the moving directions of the contact points on the rotor.

To get the closed chambers, the rotor's outline is designed to have at least three dots in contact with the inner wall of the housing at any given time. As the cusps run in a cycloidal path, the other points on the rotor's edge are also on the trajectory generated by the cusps. Thus, the outline of the rotor can be obtained through the following equations:

$$\begin{cases} e \cos t + R \cos\left(-\dfrac{t}{2} + \theta\right) = e \cos(t - 2\theta) + a \cos\left(\dfrac{2\theta - t}{2}\right) \\ e \sin t + R \sin\left(-\dfrac{t}{2} + \theta\right) = e \sin(t - 2\theta) + a \sin\left(\dfrac{2\theta - t}{2}\right) \end{cases}$$
(5)

where R is the distance of a contact point on the rotor to the rotor center, θ is the arcdegree of this point to the long axis of the rotor, and t is the rotatory angle of the output shaft. All of these parameters are shown in Fig. 10. The numerical method is used to get the coordinate positions of the points on the rotor, and the curve of the rotor's outline is fitted in the CAD software based on the numerical data. The outline fitting includes only a quarter of the rotor outline in the range of $t \in [\frac{1}{3}\pi, \pi]$, which is from the start to the end of one step. Because the rotor is symmetric about both the x and y axes, the whole outline of the rotor can be obtained from one-quarter of the outline.
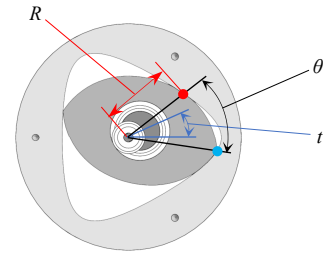

Fig. 10. Parameters of the rotor's outline.

E. Air Volume Consumption

The radius variation ratio $k = a / e$ determines the shapes of the rotor and housing. Motors with different radius variation ratios ($k = 4, 6, 8$) are shown in Fig. 11.
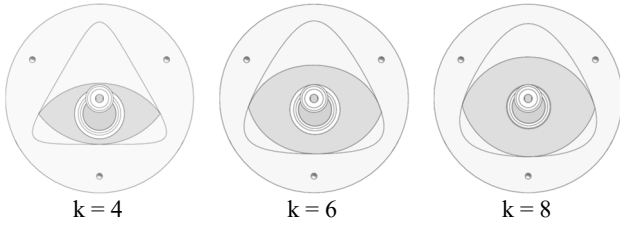
Fig. 11. Shapes of motors with different radius variation ratios.

Fig. 11 indicates that the housing with a greater radius variation ratio has a rounder outline, and the rotor is closer to a circle. Table 4 shows the chamber volumes of the motors with different radius variation ratios at the start and end positions of one step, as well as this chamber's air volume consumption. In this table, air consumption decreases along with the increase of radius variation ratio. Additionally, the air volume consumption is also affected by the lengths of the hoses.

Table 4. Air consumption of motors with different radius variation ratios

	Starting position volume (mm³)	Ending position volume (mm³)	Volume expansion (mm³)
$k = 4$	685	4052	3367
$k = 5$	705	3734	3029
$k = 6$	686	3420	2734
$k = 7$	654	3140	2486
$k = 8$	585	2891	2306

F. Multi-Chamber Motor Design

Based on the planet gear set, a series of motors are developed. Motors with different transmission ratios are shown in Fig. 12. The motor with a transmission ratio of -2 has a housing with three chambers, and its rotor has a lens shape. Similarly, the motors with transmission ratios of -3 and -4，have a 4-chamber housing and a 5-chamber housing, and their rotors are triangle-shaped and square-shaped, respectively. The 4-chamber motor and the 5-chamber motor have the same number of components as the 3-chamber motor.
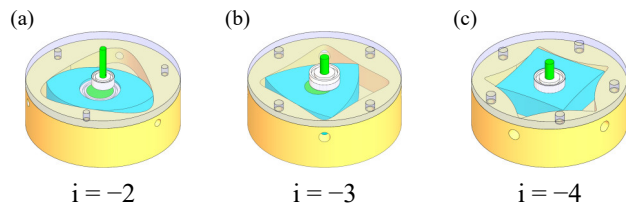

Fig. 12. Motors with different transmission ratios.

When the transmission ratio $i = -n$, the motor has $n+1$ chambers, and the trajectory of the rotor's cusps for motors with different transmission ratios can be expressed as equation (6).

$$\begin{cases} x = e \cdot \cos \alpha + a \cdot \cos \dfrac{1}{n} \alpha \\ y = e \cdot \sin \alpha - a \cdot \sin \dfrac{1}{n} \alpha \end{cases} \quad (6)$$

The 4-chamber motor (pictured in Fig. 12b) has a transmission ratio of

$$i = \frac{n_H}{n_I} = -3 \quad (7)$$

As the motor has four chambers, four hoses are needed for the transmission of compressed air into the chambers. When the compressed air fills each chamber in each step, each step can drive the rotor to rotate 30°. Thus, the output shaft runs at a resolution of 90°.

The 5-chamber motor (pictured in Fig. 12c) has a transmission ratio of

$$i = \frac{n_H}{n_I} = -4 \quad (8)$$

Five hoses are required for the motion of the transmission of compressed air into each chamber. When the compressed air fills each chamber in each step, the resolution of the motor is 72°. Additionally, the adjacent cusps of the 5-chamber motor ensure a closed chamber, so the points on the edges do not need to be in contact with the housing, which decreases the possibility of rotor edge abrasion.

When the motors are operated by only filling one chamber at a time, the motor with more chambers has greater resolution.

III. RESULTS

A. Torque and Speed Performance

In this experiment setup, Arduino Uno was used as the microcontroller to generate the signal sequence controlling the motor's rotary speed and direction. Three 4 mm outer diameter hoses were used to connect the motor and solenoid valves. The output shaft was coupled with a pulley to the motor to lift various masses. The output torque was obtained by measuring the greatest mass the motor could lift.

Fig. 13a depicts the output torque versus speed at different air pressure levels when using 1 m hoses. Torques at six different levels of air pressure were recorded, and under each air pressure, six working speeds were tested. The maximum torque was 11 mN·m at 0.48 MPa and a speed of 20 rpm.

In medical applications, the motor and solenoid valves are placed in different rooms of the MR suite. Therefore, long hoses are needed to connect the motor and valves. In this experiment, four different lengths of hoses were used to test the working speed. The motor was tested at its maximum speed until the motor stalled under the specified air pressure. Fig. 13b shows the maximum speed for different levels of air pressure and hose lengths. Two working modes were tested, 3 steps/cycle and 6 steps/cycle which were described in Fig. 6 and Fig. 7. With 0.5 m and 1 m hoses, the maximum speed decreased greatly when the motor ran at 6 steps/cycle; a possible reason for this is that the working of chamber C, described in Fig. 7a and Fig. 7b, lowered the output

efficiency. However, with the 3 m and 5 m hoses, the maximum speed did not decrease much when the motor ran at 6 steps/cycle. The maximum speed significantly decreased as the hose length increased, so the highest maximum speed of 2000 rpm was observed with the shortest (0.5 m) hoses. The maximum speed was affected by hose length because the longer the hoses are, the more time is needed for the air to propagate through the hoses. Moreover, the surface finishes of the parts, the engagement of the gear set, the diameter of hoses, and any gaps between moving parts can also influence the output torque and maximum working speed of this motor. During the experiment, the motor could not start instantly at high operating speed (over 1200 rpm with 1 m hoses), because of the inertia of the rotor and the load, so acceleration was required for high-speed motion. Similarly, deceleration was needed to bring the motor to a stop when running at high speed, as stopping the motor instantly would cause step loss and negatively impact the mechanical system.
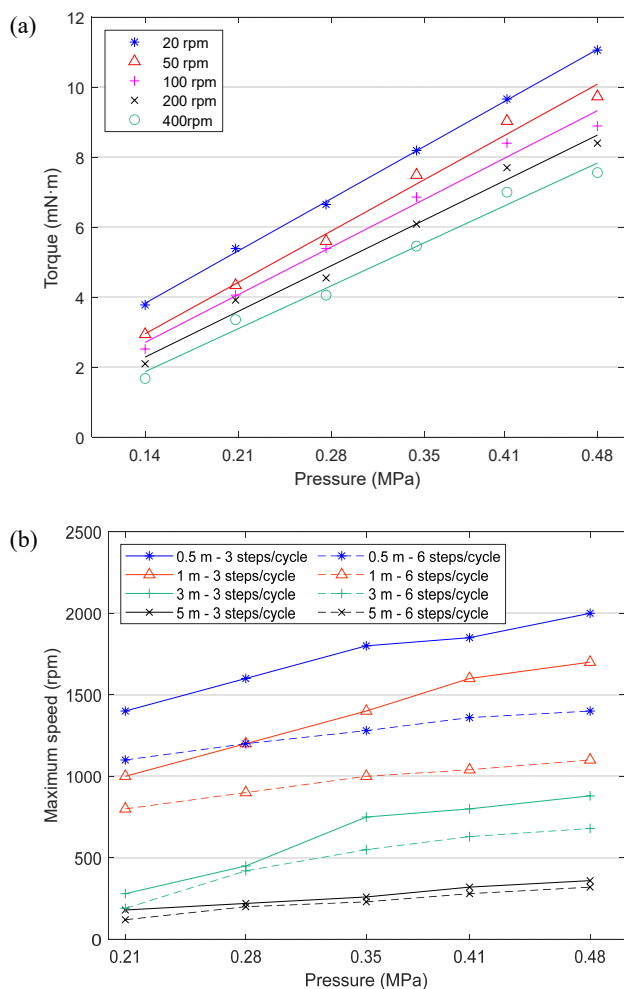

Fig. 13. (a) Output torque with respect to speed and air pressure. (b) Motor's maximum speed with respect to hose length and air pressure.

B. Position Control

In each cycle rotation, the rotor revolves a half cycle reversely, as shown in equation (4). During the first cycle and the second cycle, the orientations of the rotor are different. Thus, two cycles of output shaft rotation were tested in this experiment, resulting in a full cycle rotation of the rotor. Fig. 14 shows the position measurement of the motor running at the speed of 1 step/s with different hose lengths (1 m, 5 m, 8 m). To measure the transient position of the motor, a commercial encoder (LPD3806-600BM-G5-24C, Wisamic) with a resolution of 0.6° was coupled with the output shaft. The following observations were made.
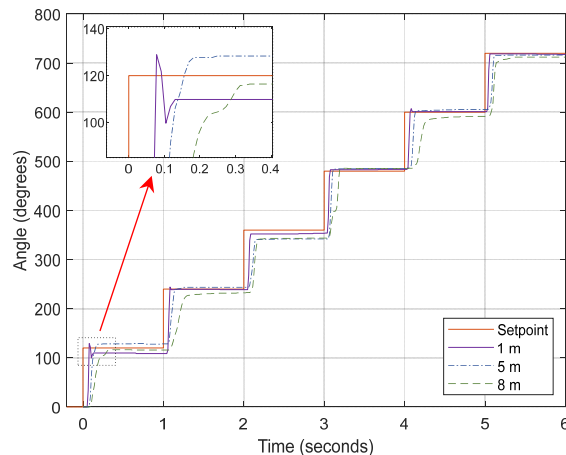

Fig. 14. Position of the motor running at 1 step/s with different hose lengths.

1) There is hysteresis between the setpoint and the actual starting position of each step. This is caused by the propagation of compressed air in the hoses. When the solenoid valve is activated, air fills the hose before reaching the chamber. The longer the hoses are, the more time is needed for air propagation, and the larger the hysteresis is. Another reason is that the inertia of the mechanism prevents the motor starting instantly.

2) The rising time increases along with the increase of the hose length. The second step (240°) and fifth step (600°) have the maximum rising time. The rotor is at the same position at these two steps, with opposite orientations. As the motor is made using 3D printing, one possible reason is that the mechanism has the largest friction at this position.

3) Some overshoots are observed at the start of the first step (120°). This is caused by the dynamics of the mechanic system; a probable explanation is that the rotor has the least friction at this position, so the rotor can pass over the setpoint and come back easily. The motor connected with 1 m hoses has the largest overshoot of 19°.

4) There is an error between the setpoint and the actual position of each step. The maximum error of 18° occurs at the third step with 5 m hoses. More error analysis is conducted in the following chapter.

C. Error Analysis

Accuracy is another critical parameter to consider when using a motor. In this test, an encoder was coupled with the output shaft, and the error was obtained by measuring the actual rotary position of each step. As the rotor rotates 360° while the output shaft rotates two cycles, the error patterns of these two cycles would be different. Therefore, target positions were set to an interval of 120° in a 720° rotation, and errors at six continuous steps were recorded for analysis. Pressured air was supplied in a sequential manner. The average error was obtained from three samples recorded at each step for the purpose of minimizing measurement error. In this study, three different levels of air pressure were chosen for testing.

From Fig. 15, it can be seen that error decreased as the pressure increased. The maximum error of one step is 25°, which is about one fifth of one step size. The error was likely caused by friction between different moving parts, such as gears and bearings. The parts are made using 3D printing, and the accuracy of the fabricated parts depends on the printing technique. The moment arm decreases when the motor runs at the end of each step, and the output torque decreases as well. Therefore, when the torque is too weak to overcome the friction resistance at the end of this step, the motor will stop. The high pressure increases the torque to overcome the friction, so the error decreases with the increase of air pressure.

The maximum error occurred at the second step (240°) for all the tested air pressures, indicating that this position had the maximum friction, so it most heavily affected the step accuracy. Besides, for the air pressure of 0.48 MPa, the error tended to be positive rather than negative like with the other air pressures. This was most likely caused by the stronger torque under higher pressure, which generates overshoot. Then, because of the friction in the motor, the rotor stops at a position over the setpoint. Finally, the error pattern of the first cycle [0, 360°] was different from that of the second cycle [360°, 720°]. At the same point of these two cycles, the shaft and rotor were at the same position, but the rotor was in different orientations. Therefore, the error difference between these two cycles was probably caused by the difference in the two lateral surfaces of the rotor, meaning the error was related to the fabrication technique.
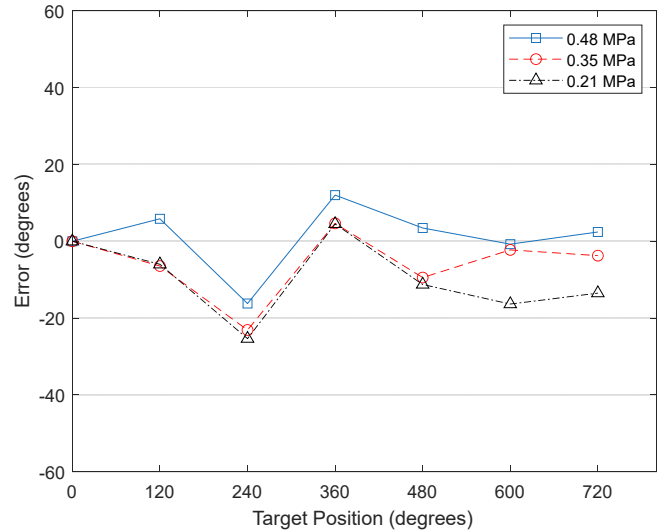

Fig. 15 Rotation accuracy at different air pressures

IV. Discussion

The most significant advantage of the proposed motor is its simple design. The cost of each motor is less than $20, including all standard parts. Higher resolution can be obtained by increasing the gear ratio to have more chambers. In cooperating with a gearbox, the resolution can be improved, and the error can be decreased as well.

The gaps between the rotor's upper face and the cover, and between the rotor's lower face and the housing, can be minimized through the use of strip seal and lubricants, and the friction caused by the seal needs to be optimized to acquire the best performance. As the trajectory of the cusps is generated by the motion of the gear set, the backlash of the gear set would influence not only the accuracy of the motor but also the trajectory of the cusps, resulting in contact force between the cusps and the inner wall of the housing. Therefore, the gaps between the cusps and the inner wall of the housing should be reserved and sealed well. Apex seals [20, 21] made of MR conditional materials which make a dynamic contact between the rotor and housing can be considered for good airtightness. The points on the rotor's outline that are in contact with the inner wall of the housing are moving along with the motion of the rotor, so material with high elasticity and lubricity could be considered. Besides sealing the mechanism, the closed-loop control of the motor can also improve the performance of the design. By utilizing both feedback and control techniques, the output torque can be increased by decreasing the speed [16].

V. Conclusion

In this work, a hypocycloid-based motor was created with the fewest parts among the listed designs. The chambers of the motor vary depending on the transmission ratio, and the resolution of the motor rises as the number of chambers increases. Furthermore, simultaneously activating the compressed air in adjacent chambers can increase the resolution. The more chambers there are, the higher the

resolution will be.

Future research will concentrate on analyzing the moving speed of the cusps in different positions alongside the inner wall, and exploring a feasible sealing method to improve the performance of the motor. As this motor is designed for use under an MR environment, future MR tests of the system driven by this motor will be conducted as well.

VI. Acknowledgments

VII. Conflict of Interest

The authors declare that the research was conducted in the absence of any commercial or financial relationships that could be construed as a potential conflict of interest. The content of this manuscript does not necessarily reflect the views, policies, or opinions of the U.S. Department of Health and Human Services nor the National Institutes of Health. The mention of commercial products, their source, or their use in connection with material reported herein is not to be construed as an actual or implied endorsement of such products by the United States government. Opinions expressed are those of the authors, not necessarily the NI.

References

[1] D. W. McRobbie, E. A. Moore, M. J. Graves, and M. R. Prince, *MRI from Picture to Proton*. Cambridge University Press, 2017.

[2] C. Nimsky, O. Ganslandt, B. von Keller, J. Romstöck, and R. Fahlbusch, "Intraoperative High-Field-Strength MR Imaging: Implementation and Experience in 200 Patients," *Radiology,* vol. 233, no. 1, pp. 67-78, 2004/10/01 2004, doi: 10.1148/radiol.2331031352.

[3] S. W. Hetts *et al.*, "Endovascular Catheter for Magnetic Navigation under MR Imaging Guidance: Evaluation of Safety In Vivo at 1.5T," *American Journal of Neuroradiology,* vol. 34, no. 11, p. 2083, 2013, doi: 10.3174/ajnr.A3530.

[4] G. S. Fischer *et al.*, "MRI-Compatible Pneumatic Robot for Transperineal Prostate Needle Placement," *IEEE/ASME Transactions on Mechatronics,* vol. 13, no. 3, pp. 295-305, 2008, doi: 10.1109/TMECH.2008.924044.

[5] Z. T. H. Tse, H. Elhawary, M. Rea, B. Davies, I. Young, and M. Lamperth, "Haptic Needle Unit for MR-Guided Biopsy and Its Control," *IEEE/ASME Transactions on Mechatronics,* vol. 17, no. 1, pp. 183-187, 2012, doi: 10.1109/TMECH.2011.2113187.

[6] K. Chinzei, R. Kikinis, and F. A. Jolesz, "MR Compatibility of Mechatronic Devices: Design Criteria," in *Medical Image Computing and Computer-Assisted Intervention – MICCAI'99*, Berlin, Heidelberg, C. Taylor and A. Colchester, Eds., 1999// 1999: Springer Berlin Heidelberg, pp. 1020-1030.

[7] A. Standard, "F2503. Standard practice for marking medical devices and other items for safety in the magnetic resonance environment," *ASTM International, West Conshohocken, PA,* 2013.

[8] H. Elhawary *et al.*, "The Feasibility of MR-Image Guided Prostate Biopsy Using Piezoceramic Motors Inside or Near to the Magnet Isocentre," in *Medical Image Computing and Computer-Assisted Intervention – MICCAI 2006*, Berlin, Heidelberg, R. Larsen, M. Nielsen, and J. Sporring, Eds., 2006// 2006: Springer Berlin Heidelberg, pp. 519-526.

[9] R. Gassert, A. Yamamoto, D. Chapuis, L. Dovat, H. Bleuler, and E. Burdet, "Actuation methods for applications in MR environments," *Concepts in Magnetic Resonance Part B: Magnetic Resonance Engineering,* https://doi.org/10.1002/cmr.b.20070 vol. 29B, no. 4, pp. 191-209, 2006/10/01 2006, doi: https://doi.org/10.1002/cmr.b.20070.

[10] J. P. Whitney, M. F. Glisson, E. L. Brockmeyer, and J. K. Hodgins, "A low-friction passive fluid transmission and fluid-tendon soft actuator," in *2014 IEEE/RSJ International Conference on Intelligent Robots and Systems*, 14-18 Sept. 2014 2014, pp. 2801-2808, doi: 10.1109/IROS.2014.6942946.

[11] C. Bergeles, P. Vartholomeos, L. Qin, and P. E. Dupont, "Closed-loop commutation control of an MRI-powered robot actuator," in *2013 IEEE International Conference on Robotics and Automation*, 6-10 May 2013 2013, pp. 698-703, doi: 10.1109/ICRA.2013.6630649. [Online]. Available: https://ieeexplore.ieee.org/stampPDF/getPDF.jsp?tp=&arnumber=6630649&ref=

[12] H. Song, K. Kim, and J. Lee, "Development of optical fiber Bragg grating force-reflection sensor system of medical application for safe minimally invasive robotic surgery," *Review of Scientific Instruments,* vol. 82, no. 7, p. 074301, 2011/07/01 2011, doi: 10.1063/1.3606502.

[13] Y. Wang, H. Su, K. Harrington, and G. S. Fischer, "Sliding Mode Control of Piezoelectric Valve Regulated Pneumatic Actuator for MRI-Compatible Robotic Intervention," 2010. [Online]. Available: https://doi.org/10.1115/DSCC2010-4203.

[14] S. Hiroyuki, K. Hiroki, K. Kenta, D. Takeyoshi, and M. Ken, "MR-Safe Pneumatic Rotation Stepping Actuator," *Journal of Robotics and Mechatronics,* vol. 24, no. 5, pp. 820-827, 2012, doi: 10.20965/jrm.2012.p0820.

[15] R. Secoli, M. Robinson, M. Brugnoli, and F. Rodriguez y Baena, "A low-cost, high-field-strength magnetic resonance imaging–compatible actuator," *Proceedings of the Institution of Mechanical Engineers, Part H: Journal of Engineering in Medicine,* vol. 229, no. 3, pp. 215-224, 2015/03/01 2015, doi: 10.1177/0954411915574306.

[16] D. Stoianovici, A. Patriciu, D. Petrisor, D. Mazilu, and L. Kavoussi, "A New Type of Motor: Pneumatic Step

Motor," *IEEE ASME Trans Mechatron,* vol. 12, no. 1, pp. 98-106, Feb 1 2007, doi: 10.1109/TMECH.2006.886258.

[17] V. Groenhuis and S. Stramigioli, "Rapid Prototyping High-Performance MR Safe Pneumatic Stepper Motors," *IEEE/ASME Transactions on Mechatronics,* vol. 23, no. 4, pp. 1843-1853, 2018, doi: 10.1109/TMECH.2018.2840682.

[18] B. L. Boland, S. Xu, B. Wood, and Z. T. H. Tse, "High Speed Pneumatic Stepper Motor for MRI Applications," *Annals of Biomedical Engineering,* vol. 47, no. 3, pp. 826-835, 2019/03/01 2019, doi: 10.1007/s10439-018-02174-0.

[19] V. Groenhuis, F. Siepel, and S. Stramigioli, "Magnetic Resonance Pneumatic Stepper Motor With Multiple Concentric Shafts Output," *IEEE/ASME Transactions on Mechatronics,* pp. 1-1, 2021, doi: 10.1109/TMECH.2021.3102024.

[20] R. Puranik and A. Akotkar, "Dynamic sealing design for Wankel Engines," *International Journal for Advance Research and Development,* vol. 4, no. 6, pp. 17-21, 2019.

[21] D.-l. Zhang *et al.*, "Theoretical Study of Seal Spring in a Wankel Compressor," presented at the 23rd International Compressor Engineering Conference, July 11-14, 2016, 1495.
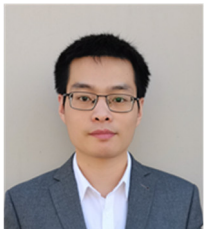
Haipeng Liang received his B.S. degree in mechanical engineering from Harbin Institute of Technology, Harbin, China. He is currently working toward the Ph.D. degree at the School of Engineering and Materials Science, Queen Mary University of London, UK. His research interests include medical robotics, MRI conditional actuators and sensors.

Zion Tsz Ho Tse is a Professor in Digital Health & Robotics at Queen Mary University of London. Prior to that, he was a Chair Professor of Medical Robotics at the University of York, an Associate Professor in the School of Electrical and Computer Engineering and an Associate Director for the Center for Cyber-Physical Systems at the University of Georgia in the USA. Before that, he was a research fellow at Harvard University, Boston, Massachusetts. His PhD degree in Mechatronics in Medicine was received from Imperial College London in the UK. Most of his academic and professional experience has been in Digital Health, Medical Mechatronics, Surgical Robotics, and Medical Imaging. He has been developing and testing a broad range of medical technologies in his career, most of which have been applied in clinical patient trials. His research bridges Engineering and Medicine, connecting multidisciplinary teams of medical doctors, researchers and engineers.